INTERNATIONAL JOURNAL FOR NUMERICAL METHODS IN FLUIDS
Int. J. Numer. Meth. Fluids 2006; **51**:197–219
Published online 15 November 2005 in Wiley InterScience (www.interscience.wiley.com). DOI: 10.1002/fld.1112

Comparisons of CIP, compact and CIP-CSL2 schemes for reproducing internal solitary waves

K. Nakayama*,†

National Institute for Land and Infrastructure Management, Yokosuka, Japan

SUMMARY

Six different models were evaluated for reproducing internal solitary waves which occur and propagate in a stratified flow field with a sharp interface. Three stages were used to compute internal solitary waves in a stratified field: (1) first-phase computation of momentum equations, (2) second-phase computation of momentum equations, which corresponds to computing the Poisson's equation, and (3) density computation. The six models discussed in this paper consisted of combinations of four different schemes, a three-point combined compact difference scheme (CCD), a normal central difference scheme (CDS), a cubic-polynomial interpolation (CIP), and an exactly conservative semi-Lagrangian scheme (CIP-CSL2). The residual cutting method was used to solve the Poisson's equation. Three tests were used to confirm the validity of the computations using KdV theory; i.e. the incremental wave speed and amplitude of internal solitary waves, the maximum horizontal velocity and amplitude, and the wave form. In terms of the shape of an internal solitary wave, using CIP for momentum equations was found to provide better performance than CCD. These results suggest one of the most appropriate scheme for reproducing internal solitary waves may be one in which CIP is used for momentum equations and CCD to solve the Poisson's equation. Copyright © 2005 John Wiley & Sons, Ltd.

KEY WORDS: CIP; CIP-CSL2; compact difference scheme; internal solitary wave; stratified field

1. INTRODUCTION

In lakes and oceans, sharp interfaces may occur due to large river inflows and strong solar radiation. In a stratified flow field with a sharp interface, external forces such as tide and wind can cause internal waves. Such internal waves play a significant role in mass transport. For example, it has been shown that internal waves and mixing drive residual circulation may transport dissolved material to the centre of a lake [1, 2].

A considerable number of field observations have been made in an effort to gain an understanding of mass transport in lakes, fjords and coastal regions resulting from internal

*Correspondence to: K. Nakayama, National Institute for Land and Infrastructure Management, Nagase 3-1-1, Yokosuka, Japan.
†E-mail: nakayama-k92y2@ysk.nilim.go.jp

Received 11 March 2005
Revised 30 June 2005
Accepted 6 September 2005

waves [3, 4]. However, the influence of internal waves on flow fields is difficult to examine through field observations because internal waves occur underwater and it is difficult to obtain high-resolution spatial data. Numerical computation is thus considered a more practical means of examining the influence of internal waves on flow fields.

The use of numerical computation to study the role of internal waves requires the use of higher-order schemes in order to reproduce sharp interfaces [5]. It is also necessary to conserve mass and energy, which are given initially, during time development. Therefore, it is necessary to use higher-order schemes that satisfy mass and energy conservation in numerical investigations of internal waves in stratified flow fields.

One approach to solving problems in a stratified flow field with a sharp interface, such as a two-layer system, is based on the Korteweg-de Vries (KdV) equation. For instance, theoretical studies of internal solitary waves have examined the nonlinear effect of the KdV [6, 7]. However, it is difficult to include completely nonlinear effects, such as the effect of an internal wave breaking, in a vertically integrated model. Therefore, models based on N-S equations that are not vertically integrated are needed to investigate mass transport caused by internal waves. For example, mass transport has been found to occur as a result of closed streamlines when large-amplitude internal waves shoal [8]. The generation of turbulence due to internal wave breaking has also been a subject of investigation in stratified flow fields [9, 10].

Computing internal waves in a stratified field can be done in three stages: (1) first-phase computation of momentum equations, (2) second-phase computation of momentum equations, which corresponds to computing Poisson's equation, and (3) density computation. Various models can then be proposed by applying different higher-order schemes to each stage.

The CIP scheme can be considered one of the most appropriate schemes in the study of internal solitary waves because the CIP scheme [11–15] is widely recognized as being a stable computation scheme for solving the advection term in the field of fluid mechanics [16]. It is semi-Lagrangian and provides high CFL conditions. The CIP scheme also provides low numerical diffusion as it solves hyperbolic equations with third-order accuracy in space [17]. This scheme is so widely applicable that it has been used to cover both compressible and incompressible flows [18] and has also been successfully applied to multi-phase flows, i.e. solid substances arising from fluids [19, 20].

The CIP-CSL family can be proposed as another scheme suitable for solving internal solitary waves because, for problems in a stratified flow field where the interface between the two layers is very thin compared to the vertical mesh size, a precise scheme that satisfies mass conservation is needed. In the CIP-CSL family, CIP-CSL4 [21–23] has been developed as an exact conservative scheme. In comparison to CIP-CSL4, the original CIP gives a more diffusive solution for a square wave advected with a constant velocity field because the conservative form is not directly solved in the advection computation [21]. A similar scheme to CIP-CSL4, CIP-CSL2 has also been developed as a conservative scheme [24, 25]. CIP-CSL4 has large memory requirements and, because of limitations on computational capacity, CIP-CSL2 will be discussed in this paper in preference to the more exact CSL4 scheme.

Amongst other potential schemes for solving internal solitary waves not already discussed, the spectral method is considered superior in reproducing internal waves [26]. The spectral method has been successfully applied to understand internal waves breaking in a stratified flow field in a simple computational domain [26]. Unfortunately, because it is difficult to apply to complicated boundary conditions, the use of the spectral method has been limited to simple flow fields. Although the flow investigated in this study could be considered simple,

a numerical scheme is needed as an alternative to the spectral method for problems with complicated boundary conditions.

Compact schemes are considered suitable alternative numerical schemes because they are highly applicable to complicated boundary conditions [27–29]. In previous studies on the development of compact schemes, a three-point combined compact difference scheme (CCD) [28, 30] was found to be one of the most accurate and widely applicable schemes because it provides sixth-order accuracy in both the interior and at the boundary. CCD can also be used to compute not only the advection term but also all other terms in space.

In this paper, six models are proposed for solving internal solitary waves. A previously developed scheme based on CIP [5] is included as one of the six models in order to understand the applicability of the new schemes and to validate the accuracy of the previously developed scheme. Each model was evaluated by comparing the results of numerical computation with theoretical solutions.

2. GOVERNING EQUATIONS

A two-dimensional large-eddy simulation model [31–33] was used to reproduce internal solitary waves in a stratified flow field with a view to using numerical computation for general problems in oceans and lakes. The two-dimensional continuity and momentum equations were:

$$\frac{\partial u_i}{\partial x_i} = 0 \tag{1}$$

$$\frac{\partial u_i}{\partial t} + u_k \frac{\partial u_i}{\partial x_k} = -\frac{1}{\rho}\frac{\partial p}{\partial x_k} + \frac{\partial}{\partial x_k}\left(\nu \frac{\partial u_i}{\partial x_k} - R_{ik}\right) + \delta_{i2}\frac{g\rho'}{\rho} \tag{2}$$

where i, $k = 1$, and 2 correspond to the coordinates of x and z, u_i ($i = 1$ and 2) are the velocities in the x and z direction t is the time, ν is the kinematic viscosity, ρ is the water density, and ρ' is the density deviation. In general, density is a function of salinity and water temperature. In this study, density was used as a variable instead of salinity and water temperature. Thus, the scalar and turbulent kinetic energy equations were:

$$\frac{\partial \rho}{\partial t} + u_k \frac{\partial \rho}{\partial x_k} = \frac{\partial}{\partial x_k}\left(K_{hk}\frac{\partial \rho}{\partial x_k}\right) \tag{3}$$

$$\frac{\partial E}{\partial t} + u_k \frac{\partial E}{\partial x_k} + \overline{u_i' u_k'}\frac{\partial u_i}{\partial x_k} = \frac{\partial}{\partial x_k}\left(K_{hk}\frac{\partial E}{\partial x_k}\right) + \delta_{i2} g \frac{1}{\rho}\overline{u_i'\rho'} - C_\varepsilon E^{3/2}/\Delta \tag{4}$$

where

$$R_{ik} = \overline{u_i' u_k'} \tag{5}$$

$$\overline{u_i' u_k'} = \delta_{i3}\frac{2}{3}E - K_{mk}\left(\frac{\partial u_i}{\partial x_k} + \frac{\partial u_k}{\partial x_i}\right) \tag{6}$$

$$\overline{u_i'\rho'} = K_{hi}\frac{\partial \rho}{\partial x_i} \tag{7}$$

$$K_{m1} = K_{m2} = C_m E^{1/2} \Delta \tag{8}$$

$$K_{h1} = C_m E^{1/2} / \mathrm{Pr} \Delta \tag{9}$$

$$K_{h2} = C_m E^{1/2} \Delta / \mathrm{Pr}_t \tag{10}$$

$$\mathrm{Pr}_t = 1 + 0.3 \Delta^2 N^2 / E \tag{11}$$

$$C_\varepsilon = 0.845 \tag{12}$$

$$C_m = 0.0856 \tag{13}$$

$$\mathrm{Pr} = 0.420 \tag{14}$$

Here, Δ is the grid length, and N is the Brunt-Vaisala frequency. The coefficient of eddy diffusion in the vertical coordinate was evaluated using second-order closure [32] to include the effects of stratification, especially around the interface.

3. COMBINED SCHEME USING CIP, CIP-CSL2, CDS, AND CCD

3.1. CIP method

The CIP scheme [11–15] is used to compute hyperbolic equations such as Euler equations:

$$\frac{\partial f}{\partial t} + u_k \frac{\partial f}{\partial x_k} = 0 \tag{15}$$

where f is an arbitrary variable. In this section, a one-dimensional hyperbolic equation and a regular grid system are dealt with in reviewing the CIP scheme. The derivative of Equation (15) yields

$$\frac{\partial}{\partial t}\left(\frac{\partial f}{\partial x_1}\right) + \frac{\partial u_1}{\partial x_1}\frac{\partial f}{\partial x_1} + u_1 \frac{\partial}{\partial x_1}\left(\frac{\partial f}{\partial x_1}\right) = 0 \tag{16}$$

Equations (15) and (16) may be divided into two computational phases as follows:
First phase:

$$\frac{f^{n+1} - f^n}{\Delta t} + u_1 \left(\frac{\partial f}{\partial x_k}\right)^n = 0 \tag{17}$$

$$\frac{1}{\Delta t}\left\{\left(\widehat{\frac{\partial f}{\partial x_1}}\right) - \left(\frac{\partial f}{\partial x_1}\right)^n\right\} + \left\{u_1 \frac{\partial}{\partial x_1}\left(\frac{\partial f}{\partial x_1}\right)\right\}^n = 0 \tag{18}$$

Second phase:

$$\frac{1}{\Delta t}\left\{\left(\frac{\partial f}{\partial x_1}\right)^{n+1} - \left(\widehat{\frac{\partial f}{\partial x_1}}\right)\right\} + \frac{\partial u_1}{\partial x_1}\left(\widehat{\frac{\partial f}{\partial x_1}}\right) = 0 \tag{19}$$

In the first phase, f^{n+1} and $(\widehat{\partial f/\partial}x_1)$ are computed using a cubic polynomial function such as

$$f_i^{n+1} = a_0\xi^3 + a_1\xi^2 + \left(\frac{\partial f}{\partial x_1}\right)^n \xi + f_i^n \tag{20}$$

$$\left(\widehat{\frac{\partial f}{\partial x_1}}\right) = 3a_0\xi^2 + 2a_1\xi + \left(\frac{\partial f}{\partial x_1}\right)^n \tag{21}$$

where i is the notation for each node, $\xi = -u_i\Delta t$, and Δx is the grid interval,

$$a_0 = 2\frac{f_i^n - f_{iup}^n}{(\Delta X)^3} + \frac{1}{(\Delta X)^2}\left\{\left(\frac{\partial f}{\partial x_1}\right)_i^n + \left(\frac{\partial f}{\partial x_1}\right)_{iup}^n\right\} \tag{22}$$

$$a_1 = 3\frac{f_{iup}^n - f_i^n}{(\Delta X)^2} - \frac{1}{\Delta X}\left\{2\left(\frac{\partial f}{\partial x_1}\right)_i^n + \left(\frac{\partial f}{\partial x_1}\right)_{iup}^n\right\} \tag{23}$$

$$\begin{cases} iup = i-1 & \Delta X = -\Delta x \quad (u_1^n \geqslant 0) \\ iup = i+1 & \Delta X = \Delta x \quad (u_1^n < 0) \end{cases}$$

$(\partial f/\partial x_1)^{n+1}$ is obtained from the known values, $\partial u_1/\partial x_1$, and $\widehat{\partial f/\partial}x_1$. In the CIP scheme, the derivative of Equation (15) is computed separately, which means that the derivative of f_i reflects the physical model described previously in Equation (16) [25].

3.2. The CIP-CSL2 scheme

The CIP-CSL2 scheme [24, 25] was proposed to satisfy mass conservation as it is not exactly satisfied in the original CIP method. A one-dimensional hyperbolic equation for mass in each grid is dealt with in the CIP-CSL2 scheme.

$$\frac{\partial D}{\partial t} + u_1\frac{\partial D}{\partial x_1} = 0 \tag{24}$$

$$D = \int_{x_i}^{x} f(x', t)\,\mathrm{d}x' \tag{25}$$

The derivative of Equation (24) yields

$$\frac{\partial}{\partial t}\left(\frac{\partial D}{\partial x_1}\right) + \frac{\partial u_k}{\partial x_k}\frac{\partial D}{\partial x_k} + u_k\frac{\partial}{\partial x_k}\left(\frac{\partial D}{\partial x_1}\right) = 0 \tag{26}$$

The same cubic polynomial function used in the CIP scheme was applied to approximate the profile of D,

$$D_i^n(x) = b_0X^3 + b_1X^2 + \left(\frac{\partial D_i}{\partial x_1}\right)^n X \tag{27}$$

where $X = x - x_i$.

The derivative of $D_i^n(x)$ was obtained as

$$F_i^n(x) = \frac{\partial D_i^n(x)}{\partial x_1} = 3b_0X^2 + 2b_1X + \left(\frac{\partial D_i}{\partial x_1}\right)^n \tag{28}$$

The coefficients, b_0 and b_1, were obtained from the boundary conditions for each mesh

$$D_i^n(x_{i+1}) = \rho_i^n \tag{29}$$

$$\frac{\partial D_i^n(x_{i+1})}{\partial x_1} = F_i^n(x_{i+1}) = f_{i+1}^n \tag{30}$$

$$\rho_i^n = \int_{x_i}^{x_{i+1}} f(x,t)\,\mathrm{d}x \tag{31}$$

Finally, the coefficients were determined as

$$b_0 = \frac{f_i^n + f_{i+1}^n}{(\Delta x)^2} - \frac{2\rho_i^n}{(\Delta x)^3} \tag{32}$$

$$b_1 = -\frac{2f_i^n + f_{i+1}^n}{\Delta x} + \frac{3\rho_i^n}{(\Delta x)^2} \tag{33}$$

The time development of ρ_i^n was obtained from the upstream volume,

$$\rho_i^{n+1} = \int_{x_i}^{x_{i+1}} f(x, t+\Delta t)\,\mathrm{d}x = \int_{x_{Pi}}^{x_{i+1}} f(x,t)\,\mathrm{d}x \tag{34}$$

where x_{Pi} is a position that moves from x_i at a speed of u_{Pi} for Δt, and x_{Pi+1} is a position that moves from x_{i+1} at a speed of u_{Pi+1} for Δt. The derivative of $D_i^n(x)$ was computed following the same procedure as for the CIP scheme.

3.3. CCD scheme

The sixth-order derivatives given by the CCD scheme were obtained from two equations [28, 30]:

$$\frac{7}{16}\left\{\left(\frac{\partial f}{\partial x_1}\right)_{i+1} + \left(\frac{\partial f}{\partial x_1}\right)_{i-1}\right\} + \left(\frac{\partial f}{\partial x_1}\right)_i - \frac{\Delta x}{16}\left\{\left(\frac{\partial^2 f}{\partial x_1^2}\right)_{i+1} - \left(\frac{\partial^2 f}{\partial x_1^2}\right)_{i-1}\right\}$$
$$= \frac{15}{16\Delta x}(f_{i+1} - f_{i-1}) \tag{35}$$

$$\frac{9}{8\Delta x}\left\{\left(\frac{\partial f}{\partial x_1}\right)_{i+1} - \left(\frac{\partial f}{\partial x_1}\right)_{i-1}\right\} + \left(\frac{\partial^2 f}{\partial x_1^2}\right)_i - \frac{1}{8}\left\{\left(\frac{\partial^2 f}{\partial x_1^2}\right)_{i+1} + \left(\frac{\partial^2 f}{\partial x_1^2}\right)_{i-1}\right\}$$
$$= \frac{3}{(\Delta x)^2}(f_{i+1} - 2f_i + f_{i-1}) \tag{36}$$

A simple iterative method was used to obtain the solution to Equations (35) and (36). CCD can compute not only the advection term but also all other terms in space.

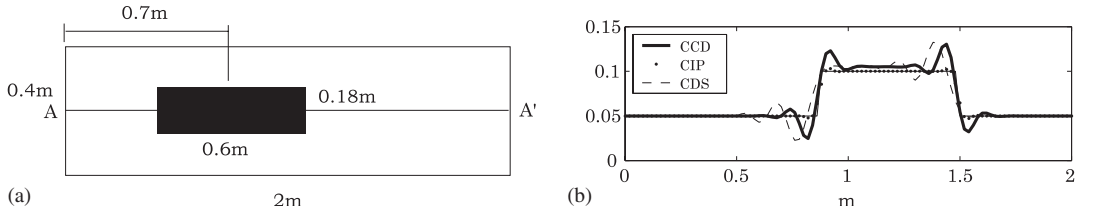

Figure 1. Two-dimensional advection problem: (a) schematic diagram of initial condition for computation; and (b) concentration along A–A′ at $t = 0.5$ s. Thin solid line indicates theoretical solution. Dots, thick line and broken line indicate the results of CIP, CCD and CDS respectively.

3.4. Two-dimensional advection problem

CCD was applied to an advection problem to investigate the characteristics of CCD in an advection computation. A two-dimensional computational domain was used by giving a constant advection velocity, $1\,\mathrm{m\,s^{-1}}$. The number of grids was taken as 100×20 with a grid interval of 0.02 m (Figure 1). The time step was given as 0.005 s and the computation was carried out for 0.5 s. The square concentration, 0.1 initially and 0.05 elsewhere, was given in a computational domain denoted by a black rectangle in Figure 1. The concentration along A–A′ was compared for CIP, CCD and CDS. Applicability to a square wave advected with a constant velocity was noticeably higher for CIP, providing important information on the computation scheme to use for density. In density computation, the scheme with the least difference between computed and actual has the highest applicability. Hence it could be suggested that density computation is best achieved through application of the CIP family. Therefore, in this study, the density computation was only conducted by using CIP family, namely CIP and CIP-CSL2.

3.5. Models

Six different models using CIP, CIP-CSL2, second-order central, and CCD schemes (denoted as CIP, CIP-CSL2, CDS, and CCD (Table I)) are proposed to reproduce internal solitary waves. The residual cutting method [34] was used to solve the Poisson's equation for all models. Turbulent kinetic energy equation was also solved by using CCD scheme for all models.

The six models can be categorized into three groups: New Models (Models 1–4), Previously Developed Model (Model 5) and Modified Previously Developed Model (Model 6). In the New Models, CCD was applied in the first phase computation of momentum equations in order to investigate differences with the Previously Developed Model (in which CIP is used). In the second-phase computation of momentum equations for the New Models, both CCD and CDS are applied. Neither CCD nor CDS schemes provided good agreement with the theoretical solution in the advection problem (previous subsection) and both are applied to make clear the high applicability of CCD compared to CDS.

In the Modified Previously Developed Model, CCD is applied in a second-phase computation of momentum equations to understand how the Previously Developed Model works compared to the modified model (which is supposed to be more accurate). As shown in the

Table I. Structure of the six models discussed in this paper, which consisted of combinations of four different schemes, a three-point combined compact difference scheme (CCD), an exactly conservative semi-Lagrangian scheme (CIP-CSL2), a cubic-polynomial interpolation (CIP), and a normal central difference scheme (CDS).

	First phase in momentum equations	Second phase in momentum equations	Density
Model 1	CCD	CDS	CIP-CSL2
Model 2	CCD	CDS	CIP
Model 3	CCD	CCD	CIP-CSL2
Model 4	CCD	CCD	CIP
Model 5	CIP	CDS	CIP
Model 6	CIP	CCD	CIP

previous subsection, the CIP family is highly applicable to density computation and only CIP and CIP-CSL2 are used in density computation for all models.

Therefore, for the momentum equations, time development for Models 1 and 2 was carried out by applying CCD to solve the first phase and using CDS to solve the Poisson's equation as follows:

First phase:

$$\frac{\hat{u}_i - u_i^n}{\Delta t} = \left(-u_k \frac{\partial u_i}{\partial x_k} - \frac{1}{\rho} \frac{\partial p}{\partial x_k} - \frac{\partial R_{ik}}{\partial x_k} + \delta_{i2} \frac{g\rho'}{\rho} + \nu \nabla^2 u_i \right)_{\mathrm{CCD}}^n \tag{37}$$

Second phase:

$$\frac{u_i^{n+1} - \hat{u}_i}{\Delta t} = -\frac{1}{\rho} \left(\frac{\partial p^{n+1}}{\partial x_k} \right)_{\mathrm{CDS}} \tag{38}$$

$$\left(\frac{\partial u_i^{n+1}}{\partial x_i} \right)_{\mathrm{CDS}} = 0 \tag{39}$$

In contrast, in Models 3 and 4, CCD was applied to solve the Poisson's equation more accurately than in Models 1 and 2 as follows:

First phase:

$$\frac{\hat{u}_i - u_i^n}{\Delta t} = \left(-u_k \frac{\partial u_i}{\partial x_k} - \frac{1}{\rho} \frac{\partial p}{\partial x_k} - \frac{\partial R_{ik}}{\partial x_k} + \delta_{i2} \frac{g\rho'}{\rho} + \nu \nabla^2 u_i \right)_{\mathrm{CCD}}^n \tag{40}$$

Second phase:

$$\frac{u_i^{n+1} - \hat{u}_i}{\Delta t} = -\frac{1}{\rho} \left(\frac{\partial p^{n+1}}{\partial x_k} \right)_{\mathrm{CCD}} \tag{41}$$

$$\left(\frac{\partial u_i^{n+1}}{\partial x_i} \right)_{\mathrm{CCD}} = 0 \tag{42}$$

The CIP scheme was applied as usual, as specified in Model 5, to investigate the differences between using CCD and CIP for momentum equations as follows:

First phase:

$$\frac{\hat{u}_i - u_i^n}{\Delta t} = \left(-\frac{1}{\rho}\frac{\partial p}{\partial x_k} - \frac{\partial R_{ik}}{\partial x_k} + \delta_{i2}\frac{g\rho'}{\rho} + \nu\nabla^2 u_i \right)_{\mathrm{CCD}}^n \tag{43}$$

Second phase:

$$\frac{\tilde{u}_i - \hat{u}_i}{\Delta t} = -\frac{1}{\rho}\left(\frac{\partial p^{n+1}}{\partial x_k}\right)_{\mathrm{CDS}} \tag{44}$$

$$\left(\frac{\partial \tilde{u}_i}{\partial x_i}\right)_{\mathrm{CDS}} = 0 \tag{45}$$

Third phase:

$$u_i^{n+1} = \mathrm{CIP}(\tilde{u}_i) \tag{46}$$

In contrast to Model 5, the CCD scheme was used to solve the Poisson's equation to improve the accuracy of computation in Model 6.

First phase:

$$\frac{\hat{u}_i - u_i^n}{\Delta t} = \left(-\frac{1}{\rho}\frac{\partial p}{\partial x_k} - \frac{\partial R_{ik}}{\partial x_k} + \delta_{i2}\frac{g\rho'}{\rho} + \nu\nabla^2 u_i \right)_{\mathrm{CCD}}^n \tag{47}$$

Second phase:

$$\frac{\tilde{u}_i - \hat{u}_i}{\Delta t} = -\frac{1}{\rho}\left(\frac{\partial p^{n+1}}{\partial x_k}\right)_{\mathrm{CCD}} \tag{48}$$

$$\left(\frac{\partial \tilde{u}_i}{\partial x_i}\right)_{\mathrm{CCD}} = 0 \tag{49}$$

Third phase:

$$u_i^{n+1} = \mathrm{CIP}(\tilde{u}_i) \tag{50}$$

Therefore, for Models 1–6, the difference between using CCD and CDS to find a solution to the Poisson's equation was determined through comparison of Models 1 and 3, Models 2 and 4, and Models 5 and 6.

For density, CIP-CSL2 was used in Models 1 and 3 as

$$d\,frac\hat{\rho} - \rho^n \Delta t = \left(\frac{\partial}{\partial x_k}\left(K_{hk}\frac{\partial \rho}{\partial x_k} \right) \right)_{\mathrm{CCD}}^n \tag{51}$$

$$\rho^{n+1} = \mathrm{CIP} - \mathrm{CSL2}(\hat{\rho}) \tag{52}$$

Table II. Models for a comparison of schemes in each phase. Corresponding figures and models discussed in the study are shown in the third column.

Compared schemes	Models	Figure (models, circle shows the model which provided better result)
CCD vs CIP for first phase	2–5 4–6	4, 8 and 12(2–⑤), 8(4–⑥)
CDS vs CCD for second phase	1–3, 2–4, 5–6	4, 5, 6, 8 and 12 (1–③, 2–④, 5–⑥, 13(①–3, ②–4, ⑤–6)
CIP-CSL2 vs CIP for density	1–2, 3–4	9 (1–2, 3–4)

Figure 4: mass conservation test
Figure 5: incremental wave speed and amplitude of an internal solitary wave (first test)
Figure 6: maximum horizontal velocity and amplitude (second test)
Figure 8: wave form (third test)
Figure 9: interface thickness
Figure 12: iteration number for computing the Poisson's equation
Figure 13: computation time

In Model 2, and Models 4–6, CIP was used as

$$\frac{\hat{\rho}-\rho^n}{\Delta t}=\left(\frac{\partial}{\partial x_k}\left(K_{hk}\frac{\partial \rho}{\partial x_k}\right)\right)^n_{\mathrm{CCD}} \tag{53}$$

$$\rho^{n+1}=\mathrm{CIP}(\hat{\rho}) \tag{54}$$

The schemes used in the study were thus evaluated as follows: (a) differences in the applicability of CCD and CIP to first-phase momentum equations were obtained by comparing Models 2 and 5, and 4 and 6; (b) the applicability of CCD to solving the Poisson's equation compared to that of CDS was determined by comparing Models 1 and 3, 2 and 4, and Models 5 and 6; (c) the influence of CIP-CSL2 on mass conservation, compared to that of CIP, was evaluated by comparing Models 1 and 2, and 3 and 4. The summary of comparisons of schemes in each phase is shown in Table II.

4. INTERNAL SOLITARY WAVE IN TWO-LAYER SYSTEM

4.1. Initial condition

We reproduced an internal solitary wave in a two-layer system to evaluate the computational performance of each model. The initial condition was selected to produce one internal solitary wave following [35, 36] (Figure 2). A configuration with light water over a deeper layer of heavier water was used. Step-like initial disturbance was created using a slightly tilted face to reduce turbulence. The difference in density between the lower and upper layers was $40\,\mathrm{kg\,m^{-3}}$. Non-slip conditions were used on both the top and bottom of the lateral walls. The number of meshes was 750×75, and the mesh intervals for each coordinate were $0.004\,\mathrm{m}\times 0.002\,\mathrm{m}$ and Δt was 0.00667 s.

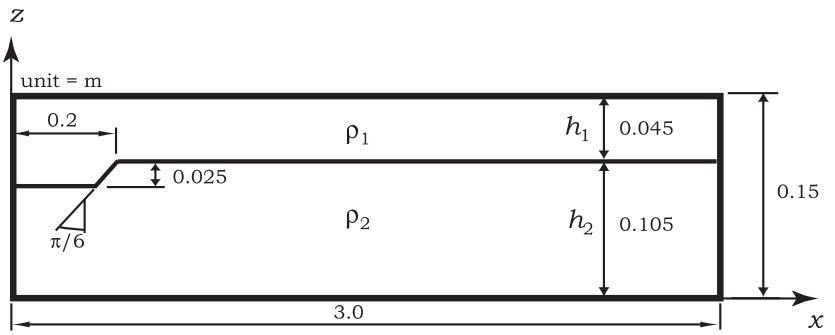

Figure 2. Schematic diagram of initial condition for computation to create one internal solitary wave. Configuration used was light water over deeper layer of heavier water. Step-like initial disturbance was created using slightly tilted face to reduce turbulence.

4.2. *Analytical solution*

A hyperbolic-tangent density profile was used to define the vertical density profile at the interface in the two-layer system.

$$\rho(z) = \rho_0 \left\{ 1 - \frac{\rho_2 - \rho_1}{2\rho_0} \tanh \alpha \left(\zeta - \frac{h_2}{h_1 + h_2} \right) \right\} \tag{55}$$

$$\zeta = z/(h_1 + h_2) \tag{56}$$

$$\rho_0 = \frac{\rho_2 + \rho_1}{2} \tag{57}$$

where ρ_1 and ρ_2 are the density of the upper and lower layers, respectively, α is a representative half-depth of the pycnocline, and ζ is along the z coordinate which starts from the bottom.

Under the Boussinesq approximation, the amplitude of an internal solitary wave is given by

$$\eta = \eta_0 \cosh^{-2} \frac{x - ct}{\lambda} \tag{58}$$

$$\frac{\lambda}{h_1} = \left\{ -\frac{6s(h_1 + h_2)}{r\tilde{c}_0\eta_0} \right\}^{1/2} \tag{59}$$

$$c = c_0 \left\{ 1 + \frac{2r\eta_0}{3(h_1 + h_2)} \right\} \tag{60}$$

$$\tilde{c}_0 = \frac{c_0}{\sqrt{g(h_1 + h_2)}} \tag{61}$$

$$r = -\frac{3\int_0^1 \rho'(\partial\phi/\partial\zeta)^3 \, \mathrm{d}\zeta}{4\int_0^1 \rho'(\partial\phi/\partial\zeta)^2 \, \mathrm{d}\zeta} \tag{62}$$

$$\frac{\partial}{\partial\zeta}\left(\rho\frac{\partial\phi}{\partial\zeta}\right) - \frac{g\phi}{c_0^2}\frac{\partial\rho}{\partial\zeta} = 0 \tag{63}$$

where $\phi(0)=\phi(1-h_2/(h_1+h_2))=0$. Equation (63) is the zeroth-order eigenvalue equation. The number of solitons that will evolve is obtained from

$$N \leqslant \frac{S}{\pi}+1 \tag{64}$$

$$s=-\frac{\tilde{c}_0 \int_0^1 \rho'\phi^2\,\mathrm{d}\zeta}{2\int_0^1 \rho'(\partial\phi/\partial\zeta)^2\,\mathrm{d}\zeta} \tag{65}$$

The number of internal solitary waves is obtained as 1 from Equation (64) which gives $N=1.4727$.

5. PERFORMANCE EVALUATION

5.1. Comparisons with analytical solution

The propagation of one dominant internal solitary wave is depicted in Figure 3, in which the number of internal solitary waves is the same as predicted from Equation (64). From the initial condition, λ, c_0, r, and s were obtained as 0.2078 m, 0.1072 m s^{-1}, -1.4124, and -0.0034, respectively. Because the propagation speed of the dominant internal solitary wave was larger than that of the other spatial high-frequency waves, the internal solitary wave propagated without being influenced by other higher frequency waves (Figure 3).

Firstly, mass conservation was investigated by comparing root mean square error of density in a tank (Figure 4). The largest errors were produced by Models 1 and 2. Interestingly, there was no significant difference between CIP and CIP-CSL2 (Models 2 and 1, and Models 4 and 3) for the density computation because the mass conservation errors were mainly caused by eddy diffusion computation using CCD. It is obvious that using CDS to solve the Poisson's equation (Models 1, 2 and 5) reduced the accuracy of mass conservation. Furthermore, the error produced by Model 5 was smaller than that produced by Model 2. The difference between Models 2 and 5 lies in the use of CIP in the first-phase computation of momentum equations in Model 5. Therefore, using CIP in momentum equations provided better mass conservation than using CCD for first-phase computation of momentum equations (Table II). This may be because CIP reflects the physical model from which the variables were derived, but CCD does not [25].

We used three tests to check the validity of the computation. As a first, the results for the incremental wave speed and amplitude of the internal solitary waves, shown in Figure 5, were compared to the theoretical solution (the solid line in Figure 5). The results from all models agreed well with the theoretical solution. Figures 4 and 5 both show a tendency towards the formation of two groups, i.e. Models 1, 2, and 5, and Models 3, 4, and 6. In Models 3, 4 and 6, CDS is used to solve the Poisson's equation. Therefore, using CDS to solve the Poisson's equation may have increased the amplitude of the internal solitary waves slightly compared to CCD (Figure 5).

In the second test, the maximum horizontal velocity and amplitude of the internal solitary waves were investigated in the second test (Figure 6). The solid line shows the theoretical solution, which produced a value of 1. Using CCD to solve the Poisson's equation (Models

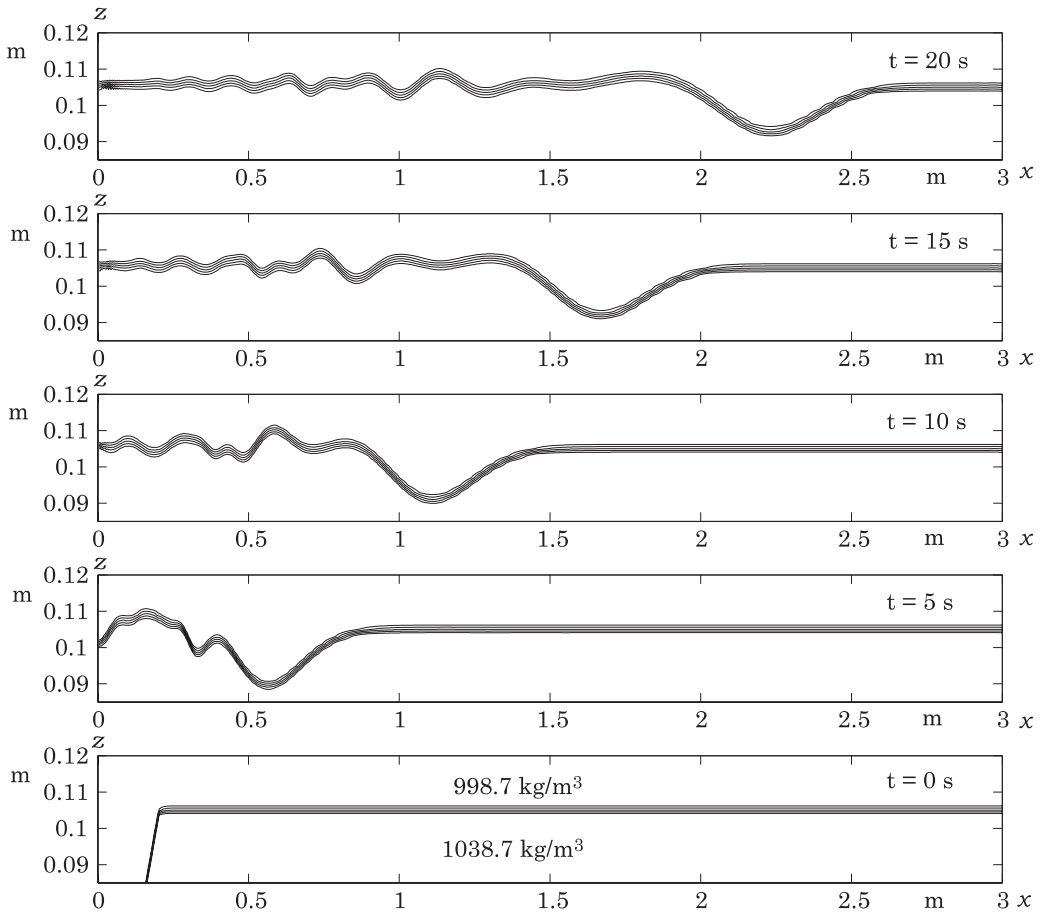

Figure 3. Contour lines with intervals of $10\,\mathrm{kg\,m^{-3}}$ every 5 s from initial condition.

3, 4 and 6) provided better results than using CDS (Models 1, 2 and 5) (Table II). As the maximum horizontal velocities were almost the same for all models, the difference between results was found to be due to the difference in the amplitude of the internal solitary waves. Therefore, the computed amplitude was found to be larger than the theoretical solution in Models 1, 2, and 5.

In the third test, the internal solitary wave form was compared with the analytical solution at $t = 20$ s (Figure 7). The solid line shows the theoretical solution and the dots show the results of computation. The root mean square error was computed to evaluate validity (Figure 8). Although all the models reproduced internal solitary waves well, results from Models 1 and 2 did not fit the theoretical solution as well as those produced by other models. Comparison of Models 2 and 5 suggests that using CIP for the advection term in the momentum equations may result in better agreement than using CCD for first-phase computation of momentum equations. Furthermore, from comparison between Models 4 and 6, using CIP for

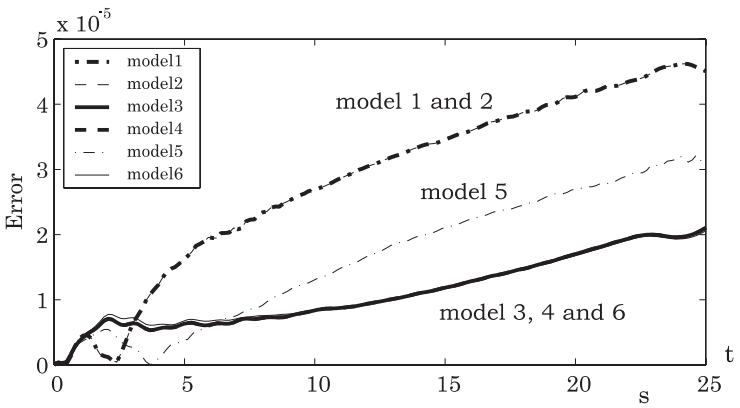

Figure 4. Time series of root mean square error of density in tank for Models 1–6.

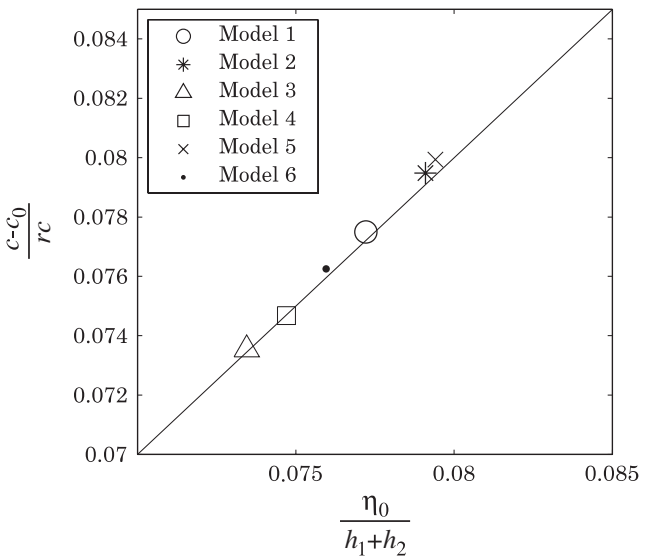

Figure 5. Incremental wave speed and amplitude of internal solitary waves for Models 1–6 showing results of computation and theoretical solution. Solid line indicates theoretical solution.

the advection term was also found to provide better result than using CCD for the first-phase computation of momentum (Table II).

In terms of density computation, the density profile and vertical gradient of density at $t = 20$ s and $x = 2.0$ m are shown on the left and right, respectively (Figure 9). The peak value for the gradient of density from CIP-CSL2 was slightly larger. However, no significant differences were found between CIP and CIP-CSL2 when interface thickness was compared.

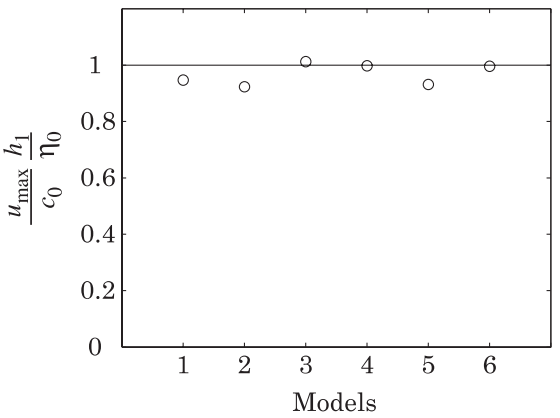

Figure 6. Maximum horizontal velocity and amplitude of internal solitary waves for Models 1–6 showing results of computation and theoretical solution. Solid line indicates theoretical solution.

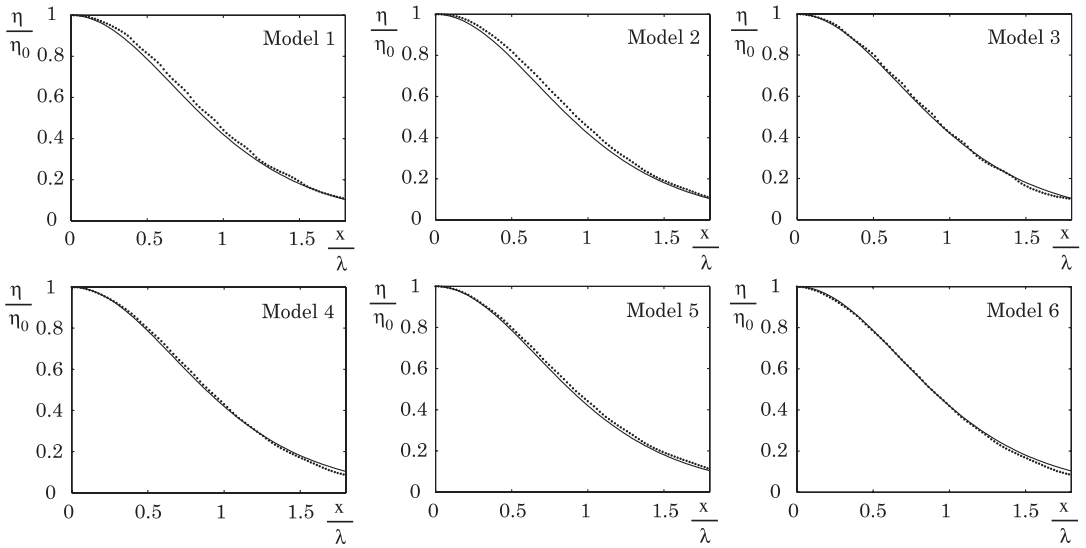

Figure 7. Internal solitary wave forms for Models 1–6 at $t = 20$ s showing results of computation and theoretical solution. Solid line indicates theoretical solution.

5.2. Evaluation of performance in solving the Poisson's equation and computation time

As discussed in Section 5.1, using CCD to solve the Poisson's equation was important in obtaining more accurate computation results. Therefore, how CCD and CDS worked in solving the Poisson's equation was investigated (Figure 10). Iterations to solve the Poisson's equation were carried out by using the residual cutting method at every time step until the root mean square error reached 10^{-6}. It was clear that the number of iterations required was more stable in Models 3, 4, and 6 than in the other models. Examples of the computed errors for each

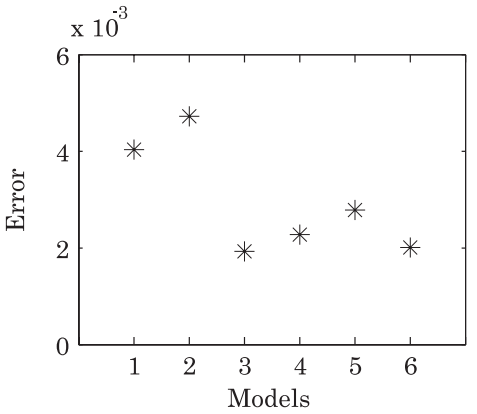

Figure 8. Root mean square error of internal solitary wave forms for Models 1–6 at $t = 20$ s.

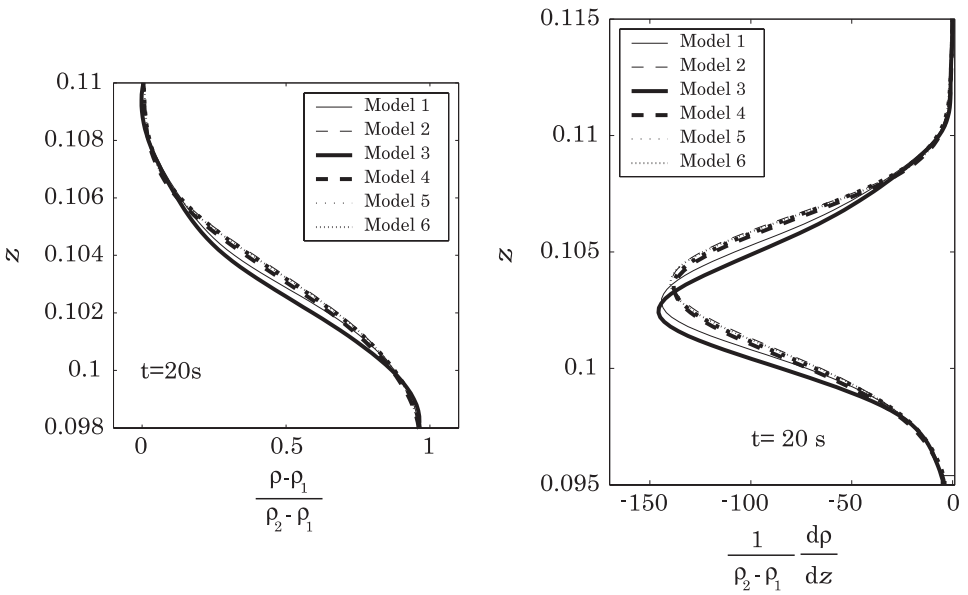

Figure 9. Vertical density profile at $t = 20$ s for Models 1–6 (left) and vertical gradient of density at $t = 20$ s for Models 1–6 (right).

model at $t = 17.12$ s are shown in Figure 11. This point in time was chosen as an example because the deformation of the internal wave shape was large and one of the largest numbers of iteration was needed to solve the Poisson's equation at $t = 17.12$ s. The necessary iteration number resulting from using CCD was smaller than using CDS. A combination of CCD and the residual cutting method may therefore be more efficient for solving the Poisson's equation.

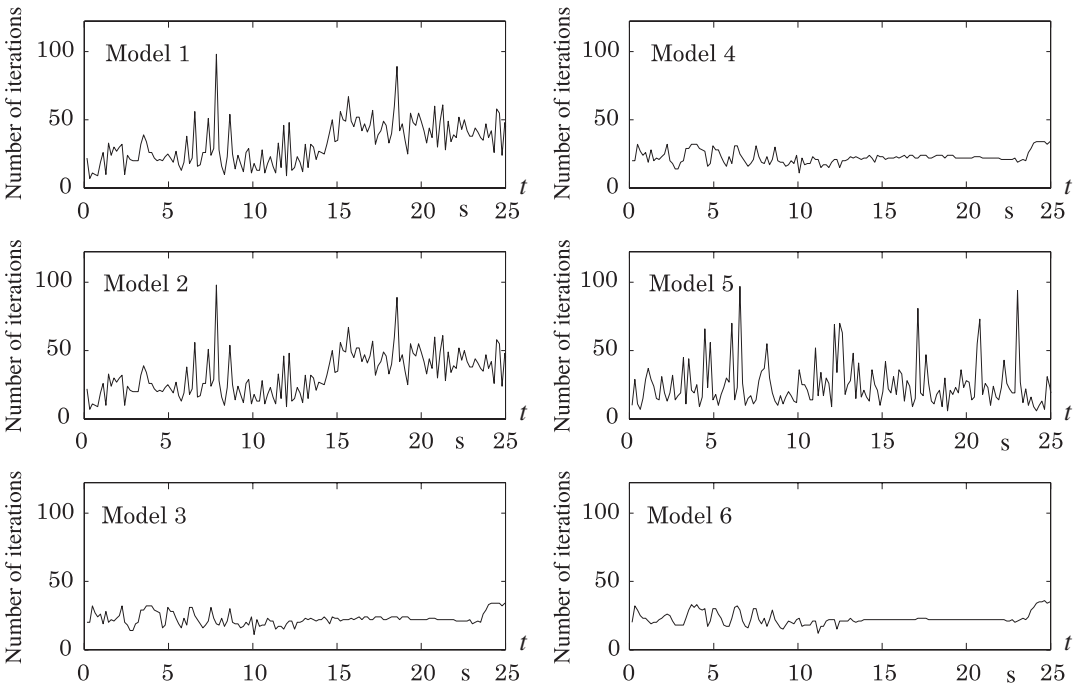

Figure 10. Time series of number of iterations until root mean square error reaches 10^{-6} for Models 1–6 when the Poisson's equation is solved.

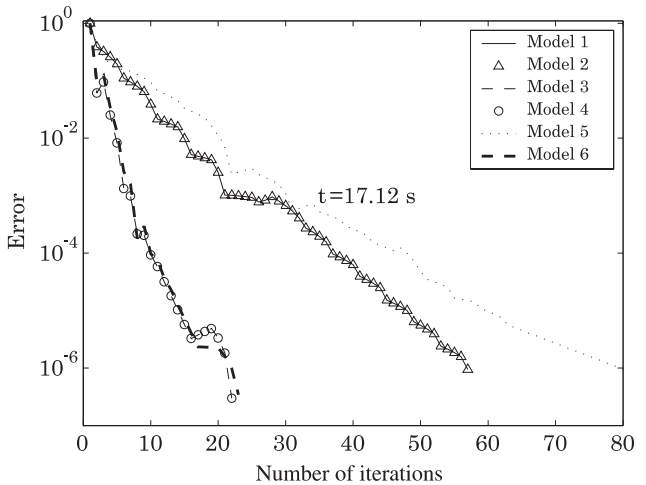

Figure 11. Root mean square error and number of iterations for Models 1–6 at $t = 17.12$ s for second-phase computation.

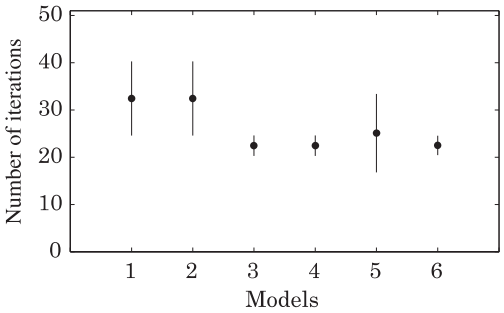

Figure 12. Average number of iterations and standard deviation for Models 1–6 from $t = 0$ to 25 s for second-phase computation.

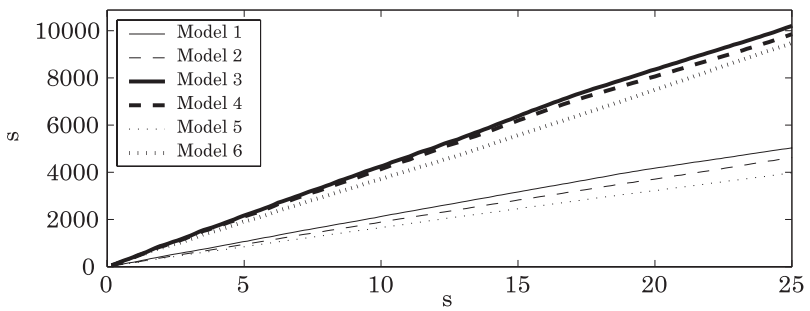

Figure 13. Comparison of actual computation time required for Models 1–6.

The average number of iterations and standard deviations are shown in Figure 12. Although the standard deviations for Models 1, 2, and 5 were larger than for the other models, the average number of iterations in Model 5 was closer to that of the models in which CCD was used to solve the Poisson's equation (Models 3, 4 and 6). The scheme used in Model 5 is generally used in a CIP scheme to solve flow in a stratified field. Therefore, comparison between Models 2 and 5 suggests that using the CIP scheme for the advection term improved the stability, even though CDS was used to solve the Poisson's equation (Table II).

Finally, the computation time required for each model was compared (Figure 13). The horizontal and vertical axes show the time taken for computation and the actual computation time, respectively. Because CCD was used to solve the Poisson's equation, the actual computation time for Models 3, 4, and 6 was almost twice as long as that for the other models.

6. CONCLUSION

Six different models, using CIP, CIP-CSL2, CCD, and CDS, were applied to reproduce an internal solitary wave in a stratified flow field, which was generated by step-like disturbance.

Propagation was considered as the initial problem. Comparisons of mass conservation showed the obvious result that using CCD to solve the Poisson's equation (Models 3, 4 and 6) produced better results than using CDS (Models 1, 2 and 5). Interestingly, using CIP to compute the advection term in the momentum equations (Model 5) provided better results than using CCD for first-phase computation of momentum equations (Model 2), which may have been because CIP reflects the physical model from which the variables were derived, but CCD does not (Figure 4 and Table II) [25].

In addition, three tests were carried out comparing the numerical computation and the theoretical solution for the incremental wave speed and amplitude of an internal solitary wave; the maximum horizontal velocity and amplitude; and the wave form. The results of the first and second tests showed that using CCD to solve the Poisson's equation (Models 3, 4 and 6) provided a good agreement with the theoretical solution for internal solitary waves. The third test showed that Model 5, in which CIP was used to compute the advection term in the momentum equations, provided better results than Model 2, in which CCD is used. Comparing the interfaces showed no significant differences between CIP and CIP-CSL2.

Using CCD to solve the Poisson's equation was found to produce more accurate results and, hence, the number of iterations and errors were evaluated for the second-phase of the momentum equations. The average number of iterations and the standard deviation were smaller when CCD was used to solve the Poisson's equation (Models 3, 4 and 6) rather than CDS (Models 1, 2 and 5).

Comparisons suggest that using CIP to compute the advection term in momentum equations produces more stable results than using CCD for first-phase computation of the momentum equations (Model 2). Therefore, Model 6, in which CIP was used in the first-phase of the momentum equation and CCD was applied to solve the Poisson's equation, may be one of the most appropriate models for studying internal solitary waves in a two-layer system. It should be noted that the applicability of this scheme to general internal wave problems requires further investigation because characteristic phenomenon, such as the breaking of internal waves, are not discussed in this study.

APPENDIX A

Model 1

First phase:

$$\frac{\hat{u}_i - u_i^n}{\Delta t} = \left(-u_k \frac{\partial u_i}{\partial x_k} - \frac{1}{\rho}\frac{\partial p}{\partial x_k} - \frac{\partial R_{ik}}{\partial x_k} + \delta_{i2}\frac{g\rho'}{\rho} + \nu\nabla^2 u_i \right)_{\mathrm{CCD}}^{n} \tag{A1}$$

Second phase:

$$\frac{u_i^{n+1} - \hat{u}_i}{\Delta t} = -\frac{1}{\rho}\left(\frac{\partial p^{n+1}}{\partial x_k}\right)_{\mathrm{CDS}} \tag{A2}$$

$$\left(\frac{\partial u_i^{n+1}}{\partial x_i}\right)_{\mathrm{CDS}} = 0 \tag{A3}$$

Density:

$$\frac{\hat{\rho}-\rho^n}{\Delta t}=\left(\frac{\partial}{\partial x_k}\left(K_{hk}\frac{\partial \rho}{\partial x_k}\right)\right)^n_{\mathrm{CDS}} \tag{A4}$$

$$\rho^{n+1}=\mathrm{CIP}-\mathrm{CSL2}(\hat{\rho}) \tag{A5}$$

Model 2
First phase:

$$\frac{\hat{u}_i-u_i^n}{\Delta t}=\left(-u_k\frac{\partial u_i}{\partial x_k}-\frac{1}{\rho}\frac{\partial p}{\partial x_k}-\frac{\partial R_{ik}}{\partial x_k}+\delta_{i2}\frac{g\rho'}{\rho}+\nu\nabla^2 u_i\right)^n_{\mathrm{CCD}} \tag{A6}$$

Second phase:

$$\frac{u_i^{n+1}-\hat{u}_i}{\Delta t}=-\frac{1}{\rho}\left(\frac{\partial p^{n+1}}{\partial x_k}\right)_{\mathrm{CDS}} \tag{A7}$$

$$\left(\frac{\partial u_i^{n+1}}{\partial x_i}\right)_{\mathrm{CDS}}=0 \tag{A8}$$

Density:

$$\frac{\hat{\rho}-\rho^n}{\Delta t}=\left(\frac{\partial}{\partial x_k}\left(K_{hk}\frac{\partial \rho}{\partial x_k}\right)\right)^n_{\mathrm{CDS}} \tag{A9}$$

$$\rho^{n+1}=\mathrm{CIP}(\hat{\rho}) \tag{A10}$$

Model 3
First phase:

$$\frac{\hat{u}_i-u_i^n}{\Delta t}=\left(-u_k\frac{\partial u_i}{\partial x_k}-\frac{1}{\rho}\frac{\partial p}{\partial x_k}-\frac{\partial R_{ik}}{\partial x_k}+\delta_{i2}\frac{g\rho'}{\rho}+\nu\nabla^2 u_i\right)^n_{\mathrm{CCD}} \tag{A11}$$

Second phase:

$$\frac{u_i^{n+1}-\hat{u}_i}{\Delta t}=-\frac{1}{\rho}\left(\frac{\partial p^{n+1}}{\partial x_k}\right)_{\mathrm{CCD}} \tag{A12}$$

$$\left(\frac{\partial u_i^{n+1}}{\partial x_i}\right)_{\mathrm{CCD}}=0 \tag{A13}$$

Density:

$$\frac{\hat{\rho}-\rho^n}{\Delta t}=\left(\frac{\partial}{\partial x_k}\left(K_{hk}\frac{\partial \rho}{\partial x_k}\right)\right)^n_{\mathrm{CDS}} \tag{A14}$$

$$\rho^{n+1}=\mathrm{CIP}-\mathrm{CSL2}(\hat{\rho}) \tag{A15}$$

Model 4
First phase:

$$\frac{\hat{u}_i - u_i^n}{\Delta t} = \left(-u_k \frac{\partial u_i}{\partial x_k} - \frac{1}{\rho}\frac{\partial p}{\partial x_k} - \frac{\partial R_{ik}}{\partial x_k} + \delta_{i2}\frac{g\rho'}{\rho} + \nu\nabla^2 u_i \right)_{\mathrm{CCD}}^{n} \tag{A16}$$

Second phase:

$$\frac{u_i^{n+1} - \hat{u}_i}{\Delta t} = -\frac{1}{\rho}\left(\frac{\partial p^{n+1}}{\partial x_k} \right)_{\mathrm{CCD}} \tag{A17}$$

$$\left(\frac{\partial u_i^{n+1}}{\partial x_i} \right)_{\mathrm{CCD}} = 0 \tag{A18}$$

Density:

$$\frac{\hat{\rho} - \rho^n}{\Delta t} = \left(\frac{\partial}{\partial x_k}\left(K_{hk}\frac{\partial \rho}{\partial x_k} \right) \right)_{\mathrm{CDS}}^{n} \tag{A19}$$

$$\rho^{n+1} = \mathrm{CIP}(\hat{\rho}) \tag{A20}$$

Model 5
First phase:

$$\frac{\hat{u}_i - u_i^n}{\Delta t} = \left(-\frac{1}{\rho}\frac{\partial p}{\partial x_k} - \frac{\partial R_{ik}}{\partial x_k} + \delta_{i2}\frac{g\rho'}{\rho} + \nu\nabla^2 u_i \right)_{\mathrm{CCD}}^{n} \tag{A21}$$

Second phase:

$$\frac{\tilde{u}_i - \hat{u}_i}{\Delta t} = -\frac{1}{\rho}\left(\frac{\partial p^{n+1}}{\partial x_k} \right)_{\mathrm{CDS}} \tag{A22}$$

$$\left(\frac{\partial \tilde{u}_i}{\partial x_i} \right)_{\mathrm{CDS}} = 0 \tag{A23}$$

Third phase:

$$u_i^{n+1} = \mathrm{CIP}(\tilde{u}_i) \tag{A24}$$

Density:

$$\frac{\hat{\rho} - \rho^n}{\Delta t} = \left(\frac{\partial}{\partial x_k}\left(K_{hk}\frac{\partial \rho}{\partial x_k} \right) \right)_{\mathrm{CDS}}^{n} \tag{A25}$$

$$\rho^{n+1} = \mathrm{CIP}(\hat{\rho}) \tag{A26}$$

Model 6
First phase:

$$\frac{\hat{u}_i - u_i^n}{\Delta t} = \left(-\frac{1}{\rho}\frac{\partial p}{\partial x_k} - \frac{\partial R_{ik}}{\partial x_k} + \delta_{i2}\frac{g\rho'}{\rho} + \nu\nabla^2 u_i \right)_{\mathrm{CCD}}^{n} \tag{A27}$$

Second phase:

$$\frac{\tilde{u}_i - \hat{u}_i}{\Delta t} = -\frac{1}{\rho}\left(\frac{\partial p^{n+1}}{\partial x_k}\right)_{\mathrm{CCD}} \tag{A28}$$

$$\left(\frac{\partial \tilde{u}_i}{\partial x_i}\right)_{\mathrm{CCD}} = 0 \tag{A29}$$

Third phase:

$$u_i^{n+1} = \mathrm{CIP}(\tilde{u}_i) \tag{A30}$$

Density:

$$\frac{\hat{\rho} - \rho^n}{\Delta t} = \left(\frac{\partial}{\partial x_k}\left(K_{hk}\frac{\partial \rho}{\partial x_k}\right)\right)^n_{\mathrm{CDS}} \tag{A31}$$

$$\rho^{n+1} = \mathrm{CIP}(\hat{\rho}) \tag{A32}$$

CCD was used to solve the turbulent kinetic energy equation for all the models.

$$\frac{E^{n+1} - E^n}{\Delta t} = \left(-u_k\frac{\partial E}{\partial x_k} - \overline{u_i' u_k'}\frac{\partial u_i}{\partial x_k} + \frac{\partial}{\partial x_k}\left(K_{hk}\frac{\partial E}{\partial x_k}\right) + \delta_{i2} g \frac{1}{\rho}\overline{u_i'\rho'} - C_\varepsilon E^{3/2}/\Delta\right)_{\mathrm{CCD}} \tag{A33}$$

REFERENCES

1. Hakanson L. Bottom dynamics in lakes. *Hydrobiologia* 1982; **9**:9–22.
2. Ostrovsky I, Yacobi YZ, Walline P, Kalikhman I. Seiche-induced mixing—its impact on lake productivity. *Limnology and Oceanography* 1996; **41**:323–332.
3. Ostrovsky LA, Stepanyants YA. Do internal solitons exist in the ocean? *Review of Geophysics* 1989; **27**:293–310.
4. Huthnance JM. Internal tides and waves near the continental shelf edge. *Geophysical and Astrophysical Fluid Dynamics* 1989; **48**:81–106.
5. Nakayama K, Okada T, Nomura M. Mechanism responsible for fortnightly modulations in estuary circulation in Tokyo Bay. *Estuarine Coast and Shelf Science* 2005; **64**:459–466.
6. Holloway PE, Pelinovsky E, Talipova T, Barnes B. A nonlinear model of internal tide transformation on the Australian North West Shelf. *Journal of Physical Oceanography* 1997; **27**:871–898.
7. Horn DA, Imberger J, Ivey GN. The degeneration of large-scale interfacial gravity waves in lakes. *Journal of Fluid Mechanics* 2001; **434**:181–207.
8. Lamb KG. A numerical investigation of solitary internal waves with trapped cores formed via shoaling. *Journal of Fluid Mechanics* 2002; **451**:109–144.
9. Andreassen O, Hvidsten PO, Fritts DC, Arendt S. Vorticity dynamics in a breaking internal gravity wave. Part 1. Initial instability evolution. *Journal of Fluid Mechanics* 1998; **367**:27–46.
10. Andreassen O, Hvidsten PO, Fritts DC, Arendt S. Vorticity dynamics in a breaking internal gravity wave. Part 1. Vortex interactions and transition to turbulence. *Journal of Fluid Mechanics* 1998; **367**:47–65.
11. Takewaki H, Nishiguchi A, Yabe T. Cubic interpolated pseudoparticle method (CIP) for solving hyperbolic type equations. *Journal of Computational Physics* 1985; **61**:261–268.
12. Takewaki H, Yabe T. The cubic-interpolated pseudo particle (CIP) method: application to nonlinear and multi-dimensional hyperbolic equations. *Journal of Computational Physics* 1987; **70**:355–372.

13. Yabe T, Aoki T. A universal solver for hyperbolic equations by cubic-polynomial interpolation. I. One-dimensional solver. *Computer Physics Communications* 1991; **66**:219–232.
14. Yabe T, Ishikawa T, Wang PY, Aoki T, Kadota Y, Ikeda F. A universal solver for hyperbolic equations by cubic-polynomial interpolation. II. Two- and three-dimensional solver. *Computer Physics Communications* 1991; **66**:233–242.
15. Yabe T, Takizawa K, Chino M, Imai M, Chu CC. Challenge of CIP as a universal solver for solid, liquid and gas. *International Journal for Numerical Methods in Fluids* 2005; **47**:655–676.
16. Bui VA, Dinh TN, Sehgal BR. Numerical simulation of interface phenomena using CIP and the level set front-capturing method. *Computational Fluid Dynamics Journal* 1991; **8**(1):103–112.
17. Utsumi T, Kunugi T, Aoki T. Stability and accuracy of the cubic interpolated propagation scheme. *Computer Physics Communications* 1997; **101**:9–20.
18. Suzuki K, Fujimatsu N. Application of CIP method to viscous supersonic and hypersonic flow analysis around aerospace vehicles. *Computational Fluid Dynamics Journal* 1999; **8**(1):113–120.
19. Xiao F, Ebisuzaki T. Parallel implementation of a computational code for complex flows. *Computational Fluid Dynamics Journal* 1999; **8**(1):13–18.
20. Nakamura T, Yabe T. Cubic interpolated propagation scheme for solving the hyper-dimensional Vlasov–Poisson equation in phase space. *Computer Physics Communications* 1999; **120**:122–154.
21. Yabe T, Tanaka R, Nakamura T, Xiao F. An exactly conservative semi-Lagrangian scheme (CIP-CSL) in one dimension. *Monthly Weather Review* 2000; **129**:332–344.
22. Takizawa K, Yabe T, Nakamura T. Multi-dimensional semi-Lagrangian scheme that guarantees exact conservation. *Computer Physics Communications* 2002; **148**:137–159.
23. Xiao F, Yabe T, Peng X, Kobayashi H. Conservative and oscillation-less atmospheric transport schemes based on rational functions. *Journal of Geophysical Research* 2002; **107**(D22):4609.
24. Nakamura T, Tanaka R, Yabe T, Takizawa K. Exactly conservative semi-Lagrangian scheme for multi-dimensional hyperbolic equations with directional splitting technique. *Journal of Computational Physics* 2001; **174**:171–207.
25. Tanaka R, Nakamura T, Yabe T. Constructing an exactly conservative scheme in a non-conservative form. *Computer Physics Communications* 2000; **126**:232–243.
26. Andreassen O, Wasberg CE, Fritts DC, Isler JR. Gravity wave breaking in two and three dimensions 1. Model description and comparison of two-dimensional evolutions. *Journal of Geophysical Research* 1994; **99**:8095–8108.
27. Lele SK. Compact finite difference schemes with spectral-like resolution. *Journal of Computational Physics* 1991; **103**:16–42.
28. Chu PC, Fan C. A three-point combined compact difference scheme. *Journal of Computational Physics* 1998; **140**:370–399.
29. Nihei T, Ishii K. A fast solver of the shallow water equations on a sphere using a combined compact difference scheme. *Journal of Computational Physics* 2003; **187**:639–659.
30. Chu PC, Fan C. A three-point sixth-order nonuniform combined compact difference scheme. *Journal of Computational Physics* 1999; **148**:663–674.
31. Lilly DK, Waco DE, Adelfang SI. The representation of small-scale turbulence in numerical simulation experiments. *Proceedings IBM Science. Computation Symposium on Environmental Science* 1967; 195–210.
32. Schmidt H, Schumann U. Coherent structure of the advection boundary layer derived from large-eddy simulations. *Journal of Fluid Mechanics* 1989; **200**:511–562.
33. Schumann U. Subgrid length-scales for large-eddy simulation of stratified turbulence. *Theoretical Computational Fluid Dynamics* 1991; **2**:279–290.
34. Tamura A, Kikuchi K, Takahashi T. Residual cutting method for elliptic boundary value problems. *Journal of Computational Physics* 1997; **137**:247–264.
35. Kao TW, Pan FS, Renouard D. Internal solitions on the pycnocline: generation, propagation, and shoaling and breaking over a slope. *Journal of Fluid Mechanics* 1985; **159**:19–53.
36. Michallet H, Ivey GN. Experiments on mixing due to internal solitary waves breaking on uniform slopes. *Journal of Geophysical Research* 1999; **104**:13467–13477.

